DOI:
10.1021/acs.nanolett.6b05026

Document Version
Peer reviewed version

Bridging the gap between dielectric nanophotonics and the visible regime with effectively lossless GaP antennas

Journal:	*Nano Letters*
Manuscript ID	nl-2016-05026y.R1
Manuscript Type:	Communication
Date Submitted by the Author:	16-Jan-2017
Complete List of Authors:	Cambiasso, Javier; Imperial College London, Physics Grinblat, Gustavo; Imperial College London, Physics Li, Yi; Imperial College London, Blackett Laboratory Rakovich, Aliaksandra; Imperial College London, Physics Department Cortés, Emiliano; Imperial College London, Physics Maier, Stefan; Imperial College, Physics;

Bridging the gap between dielectric nanophotonics and the visible regime with effectively lossless GaP antennas

Javier Cambiasso, Gustavo Grinblat, Yi Li, Aliaksandra Rakovich, Emiliano Cortés,* and Stefan A. Maier*

The Blackett Laboratory, Imperial College, Prince Consort Road, London, SW7 2BB

E-mail: e.cortes@imperial.ac.uk; s.maier@imperial.ac.uk

Abstract

We present all-dielectric gallium phosphide (GaP) nanoantennas as an efficient nanophotonic platform for surface-enhanced second harmonic generation (SHG) and fluorescence (SEF), showing negligible losses in the visible range. Employing single GaP nanodisks, we observe an increase of more than three orders of magnitude in the SHG signal in comparison with the bulk. This constitutes an SHG efficiency as large as 0.0002%, which is, to the best of our knowledge, the highest yet achieved value produced by a single nano-object in the optical region. Furthermore, we show that GaP dimers with 35 nm gap can enhance up to 3600 times the fluorescence emission of dyes located in the gap of the nanoantenna. This is accomplished by a fluorescence lifetime reduction of, at least, 22 times, accompanied by a high intensity field confinement in the gap region. These results open new avenues for low-loss nanophotonics in the optical regime.

Keywords

gallium phosphide, dielectric nanoantennas, second harmonic generation, fluorescence enhancement, Purcell effect

Main

The initial excitement on metallic nanostructures for the production of nanophotonic devices operating in the visible regime was later partially eclipsed with the realization that losses could play a role as important as that of the actual radiative properties. [1–5] Losses have been, however, exploited in other useful ways, [6–9] for example by making use of the highly localized heat, [10] by utilizing the generated hot-electrons to induce highly localized photocurrents, [11] or to drive chemical reactions at desired nanoscale regions, [8,9,12–14] among others. In this context, dielectric nanoantennas emerge as complementary candidates to plasmonic systems. Nanostructured high-refractive index dielectrics can highly confine electric and magnetic fields at subwavelength volumes, [15] while presenting ultra-low absorption −compared to metals− when excited above their bandgap energies. As such, they could be considered as an alternative to overcome the current limitations of plasmonic nanoantennas.

At this point, it is important to clarify the different underlying physical phenomena between the widely used dielectric microcavity and the novel concept of the dielectric nanoantenna: while microresonators use high Q-factors to generate field enhancements, [16,17] nanoantennas use small modal volumes with low Q-factors, broadening the spectral range of operation, while reducing field-enhanced region volumes. GaP, in particular, has an associated bandgap wavelength as small as $<$550 nm with a refractive index of $\sim$3.3, opening interesting opportunities for the realization of low-loss nanophotonic antennas in the optical regime. [18]

Recently, applications such as second or third harmonic generation as well as surface enhanced Raman or fluorescence spectroscopy were explored by exploiting the ability of high-refractive index nanoantennas to highly confine the electric field at subwavelength volumes

[2,15,16,19–21]. Indeed, since the efficiency of nonlinear phenomena and the enhancement factors of surface-enhanced spectroscopies increase with the excitation density, locally enhancing the incident light intensity can significantly amplify these processes.

Second harmonic generation (SHG), particularly, is a coherent nonlinear phenomenon that converts two photons of frequency ω into one photon of frequency 2ω. On the macroscopic scale, the crystal symmetry of the excited structure has to be non-centrosymmetric in order to produce a non-zero SHG signal, as SHG is a second order process.[22] In the nanometer scale, however, inhomogeneities in the fields or in the materials may induce a high second order nonlinear response, even for structures with a centrosymmetric crystal lattice.[22–24] Based on this property, in the past decade, different configurations of plasmonic nanoantennas have been engineered to produce second harmonic (SH) conversion efficiencies (η^*_{SH}) of up to $10^{-6}\%$.[25–27] Nonetheless, the large absorption of the metallic nanostructure when excited at the plasmonic resonance severely limits the amount of power that can be delivered to the nanosystem without damaging the material or changing its refractive index,[3] preventing the possibility of achieving higher η^*_{SH} values. To address this issue, very recently, low-loss dielectric nanoantennas made from Si, Ge and AlGaAs have been used instead, demonstrating promising results for second and third harmonic generation [19,28–32]. Specifically for SHG, AlGaAs nanoantennas have been shown to produce η^*_{SH} values as large as $\sim 10^{-3}\%$ for SH wavelengths in the near infrared.[30] However, up to now, this strategy has not yet been adopted to generate efficient SH light in the visible range, mainly due to the relatively large absorption that most high-refractive index dielectrics present in this spectral regime.[33] Therefore, GaP, which has an absorption coefficient that can be up to more than three orders of magnitude lower than those of Au, Ag and AlGaAs at optical frequencies,[34–36] emerges as a promising candidate for visible SHG [37–39].

Following this scenario, a GaP nanoantenna could also be considered as a potential alternative to plasmonic systems [40] for surface enhanced fluorescence (SEF), since all standard fluorophores absorb and emit in the visible range. Indeed, ohmic losses and quenching effects,

typically present in metal structures, would be completely avoided in GaP nanoantennas for excitation wavelengths above their bandgap (*i.e.* >550 nm). Regarding reported research on dielectric nanoantennas for SEF, up to now, only Si dimers with nanoscale gaps have been investigated for this purpose, reaching fluorescent enhancement values ranging from 250 to 2000 when placing the fluorescent molecules in their gaps.[16,21] It is worth mentioning that even though Si does absorb light in the visible regime, its absorption coefficient is nearly two orders of magnitude lower than that of Au.[36] However, the remaining absorption of Si is still one order of magnitude larger than that of GaP[41] (see Supporting Information, section 1), and therefore represents a limitation for fluorescent enhancement, with non-negligible non-radiative contributions.[21] In this context, GaP could then boost radiative emission even more than Si.

In this Letter, we exploit the properties of GaP nanoantennas as an effectively lossless nanophotonic platform at optical frequencies, and show its applicability for both resonantly enhanced SHG and SEF. We start by showing efficient generation of SH light throughout the visible range by tuning the size of single GaP nanodisks (NDs), enhancing their nonlinear response by more than three orders of magnitude with respect to the bulk. Afterwards, we probe the properties of fluorescent molecules located in the hot-spot of a GaP dimer nanoantenna, attaining a fluorescence enhancement factor of 3600 when comparing with the bare emitter. Both, high-field confinement effects, and a fluorescence lifetime reduction of more than one order of magnitude, produced the observed SEF factor when placing the molecules within the 35 nm gap.

Different designs of GaP nanoantennas of 200 nm height (h) were fabricated by masking a GaP substrate using electron-beam lithography, followed by several wet and dry etching steps (more fabrication details can be found in the SI, section 2). Two masking layers were used to improve the sidewall homogeneity. We start by considering the simple case of the single nanodisk (ND), which has been recently demonstrated[39] as a convenient geometry for the enhancement of harmonic generation efficiencies when using dielectrics such as Si, Ge,

and AlGaAs.[19,28–30] However, to the best of our knowledge, the dielectric ND has not yet been investigated for SHG in the visible range. To address this issue, we chose to study the SHG characteristics of individual GaP NDs of h = 200 nm in this spectral region (schematic and scanning electron micrograph image in Figure 1(a)).

Following fabrication, to determine resonance wavelengths, we numerically calculated and experimentally measured the scattering cross section spectra of NDs of different radii R, in the range of 200 to 400 nm. Relevant geometrical parameters of the nanostructures, as deduced from scanning electron micrographs, as well as the refractive index of (bulk) GaP, determined through ellipsometry (refer to SI, section 1, for ellipsometry data), were used as input values for the simulations. Figures 1(b)-(c) show, respectively, the simulated and experimental scattering cross section spectra for the case of the smallest ND, with R = 200 nm. In both cases a single peak appears in the selected spectral region, indicating the presence of a resonant mode. The observed $\sim$ 10% disagreement in the experimental resonance frequency with respect to the numerical calculation, a discrepancy commonly observed in high refractive index nanophotonics,[19,42,43] may be attributed to tapered walls, rounding effects and superficial debris in the real nanoantennas that deviate the fabricated disk from the assumed perfect cylindrical geometry.

To gain better understanding of the resonance registered in the scattering cross section spectrum, in Figure 1(d) we plot its associated electric field intensity distribution in the vicinity of the nanoantenna. It can be seen that the electric field is highly confined to the top and lateral surfaces of the ND, with enhancement factors around 30. This mode shows a strong quadrupolar magnetic resonance, as inferred from the simulated magnetic field intensity distribution, included in the SI, section 3. Even though the bulk contribution to second order nonlinear processes is expected to be negligible,[38] by concentrating the electric field intensity to the surfaces, this mode could enable efficient SHG. Indeed, the GaP crystal structure behaves effectively as centrosymmetric when the direction of the light polarization is contained within the fundamental planes of the zinc blende (cubic) lattice (100), (010)

or (001), as in our experimental conditions, in contrast to, for example, the case of non-centrosymmetric GaP (110).[39,44]

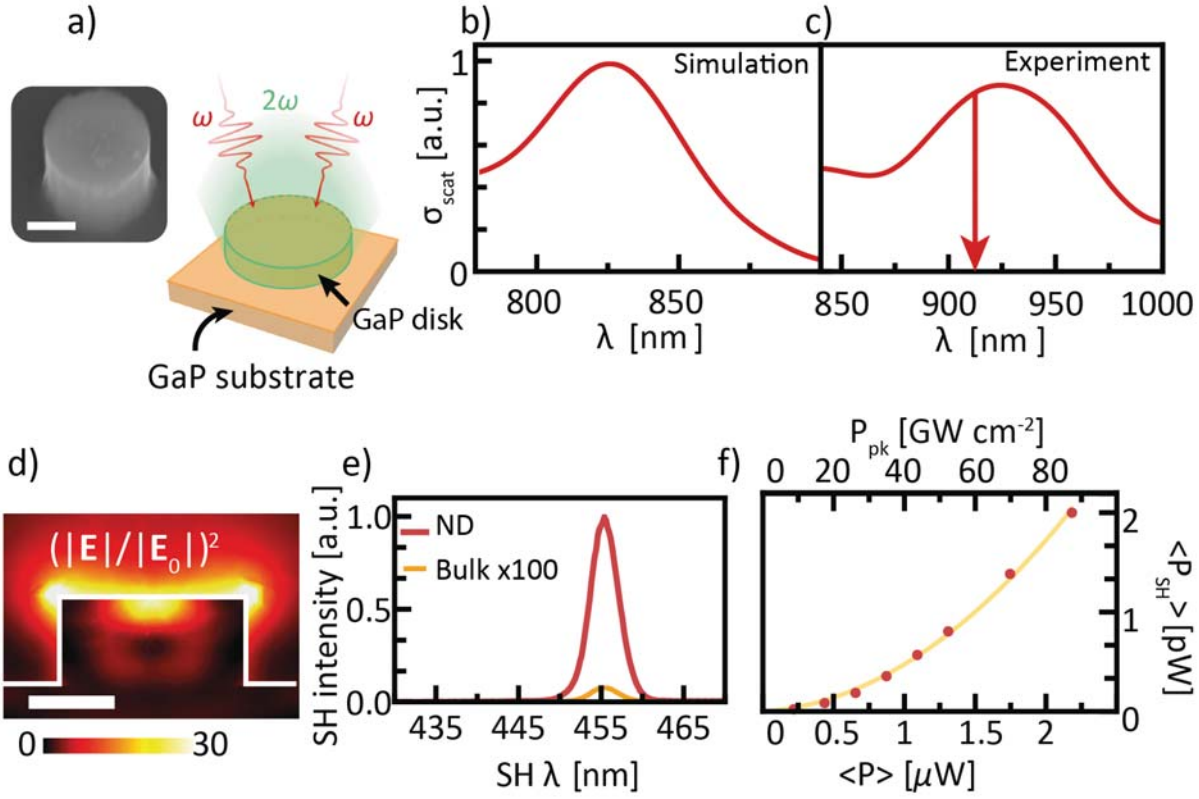

Figure 1: (a) Scanning electron micrograph of a 200 nm radius disk. Scale bar: 200 nm. Schematic view of the experimental setup for a disk emitting green SH light. (b)-(c)Simulated (b) and experimental (c) scattering cross section spectrum of a single 200 nm thick GaP ND with $R = 200$ nm. The vertical arrow in (c) represents the chosen excitation wavelength band for the nonlinear characterization. (d) XZ cross section of the predicted electric field intensity distribution computed at the simulated scattering maximum. Scale bar: 200 nm. (e) SH spectra of the ND and bulk GaP substrate for an excitation wavelength of 910 nm. (f) Dependence of the average SH power $\langle P_{\mathrm{SH}} \rangle$ with the average excitation power $\langle P \rangle$ for the ND. The solid line is a fit of the data considering the expected quadratic dependence of $\langle P_{\mathrm{SH}} \rangle$ with $\langle P \rangle$.

In Figure 1(e), the SH spectrum of a single GaP ND and that of the GaP substrate (bulk) are shown for an excitation wavelength of 910 nm, *i.e.* at the resonance wavelength as evidenced from the measured scattering cross section spectrum (Figure 1(c)). The description of the experimental setup employed for the nonlinear characterization can be found in the SI, section 4. As expected, the SH spectra show, in both cases, a single peak centered at 455

nm, which is half of the excitation wavelength. Moreover, a remarkable enhancement of 1300 times is found in the SH emission signal for the ND with respect to the substrate. Our theoretical calculation of the SH enhancement factor, which considers surface SH nonlinearity, also supports this result. First, we can rule out the contributions from the optical response of the nanoantenna at the SH frequency since no resonances were found at this wavelength in the scattering cross section spectrum. Then, it is necessary to consider the electric field intensity enhancement of ∼30 at the registered scattering resonance (Figure 1(d)), together with the factor of $1+2\times h/R=3$ determined by the increased surface area of the ND when compared to unstructured GaP. Since the field enhancement is only localized at the top quarter part of the disk, these contributions combined give rise to a predicted enhancement factor of about $30^2 \times (1+2/4) = 1350$ in the SH power, which matches very well the one obtained experimentally.

To reveal the dependence of the SH signal with the excitation density, we experimentally measured fundamental and harmonic powers in the range of 0-100 GW cm^{-2} peak pump intensity, as exhibited in Figure 1(f). The results show the expected trend of the SH intensity increasing quadratically with the pump power, as described by the second order polynomial fit. In order to calculate the corresponding SH conversion efficiencies, we use the usual equations[26,45] $\eta_{\mathrm{SH}} = P_{\text{pk-SH}}/P_{\mathrm{pk}}^2$ ($P_{\text{pk-SH}}$, peak SH power; P_{pk}, peak pump power), which yields a value as high as 0.4% MW^{-1}, and $\eta_{\mathrm{SH}}^* = P_{\text{pk-SH}}/P_{\mathrm{pk}} = \eta_{\mathrm{SH}} \times P_{\mathrm{pk}}$, which expresses the percentage of incident light converted into SH emission, and increases linearly with the power of the fundamental wave. In particular, at $P_{\mathrm{pk}} = 200$ GW cm^{-2}, which is the maximum power we could input without damaging the sample, we obtain a value of η_{SH}^* of 0.0002%. To the best of our knowledge, this is the highest SH conversion efficiency reported so far for a single nanoscale object at optical frequencies, exceeding by several orders of magnitude those reported for monomer and dimer-like metallic nanoantennas,[25–27] and by one order of magnitude that reported for a hybrid Au/ZnO nanoantenna.[46] Moreover, our experimental results demonstrate that the Mie-resonant GaP ND is considerably more efficient than the

recently investigated micrometer-long GaP nanopillar waveguide,[38,39] which provides η^*_{SH} values of only $\sim 10^{-7}\%$. It is essential to mention here that excitation powers as high as $P_{pk} = 200$ GW cm^{-2} were only possible due to the ultra-low absorption of GaP. Indeed, typical maximum P_{pk} values for resonant Si or Ge nanoantennas are two orders of magnitude lower than the ones used here for GaP.[19,28,30]

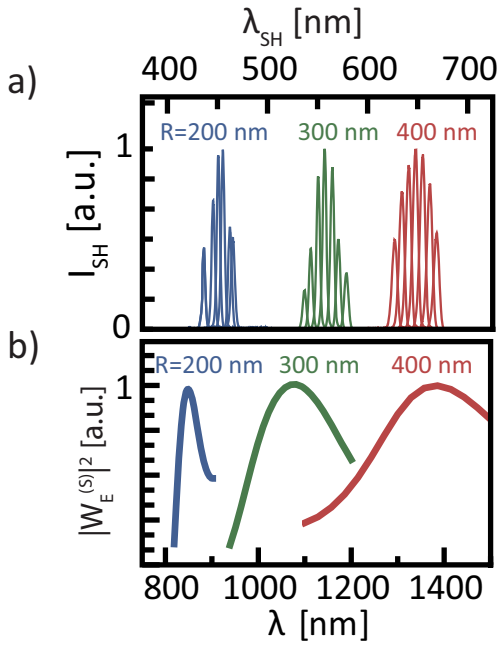

Figure 2: (a) Experimentally obtained fundamental wavelength dependence of the SH spectrum for radii (R) of 200 nm (blue spectra), 300 nm (green spectra), and 400 nm (red spectra). The sets of curves are normalized to have equal maximum intensity. Each spectrum corresponds to a different fundamental wavelength of double that of the central SH wavelength. Full width at half maximum of each spectrum is ∼5 nm. (b) Simulated spectral dependence of the square of the surface electric energy for the three different ND radii.

In order to demonstrate efficient SH emission over the entire visible range, we also examine the nonlinear characteristics of NDs with larger diameters. Keeping the thickness fixed at 200 nm, Figure 2(a) shows the measured nonlinear optical response corresponding to NDs with R values of 200 nm, 300 nm and 400 nm when varying the excitation wavelength. It can be seen that while the smallest nanoantenna produces maximum SHG at ∼450 nm wavelength

(blue), as expected, the NDs of 300 nm and 400 nm radii generate optimum SH emission at $\sim$ 550 nm (green) and $\sim$ 650 nm (red) wavelengths, respectively. Furthermore, the conversion efficiencies measured for the green and red SHG are comparable to that obtained for blue light, *i.e.* $\eta^*_{\mathrm{SH}} \sim 10^{-4}\%$ for the whole visible range. Concerning the dependence of the conversion efficiency on the polarization of the fundamental wave, since the structure presents rotational symmetry about the z-axis, any polarization direction parallel to the substrate surface plane would produce equal SH intensity. However, components with polarization perpendicular to this direction would fail to excite the simulated mode in Figure 1(d), which assumes normal incidence only. In our experimental configuration, since most of the focused beam is linearly polarized in the x-direction, efficient excitation of this resonant mode is expected.

For the purpose of understanding the SH spectral response in Fig. 2(a), we calculate the electric energy stored at the surface of the ND, $W_E^{(S)} = n^2/2 \iint \|\mathbf{E}(\mathbf{r},\lambda)\|^2 \,\mathrm{d}S$. Essentially, since SHG is a second order process that behaves as a surface phenomenon under our experimental conditions, the electric energy at the nanostructure surface at the fundamental wavelength can be used to represent the excitation power. At the same time, the observed variations in the SH emission intensity as the fundamental wavelength is scanned can be associated with the corresponding variations in $\left|W_E^{(S)}\right|^2$. Indeed, as observed in Fig. 2(b) for all different R values, the spectral dependence of $\left|W_E^{(S)}\right|^2$ describes well the corresponding measured spectral dependence of the SH signal shown in Figure 2(a). While a similar concept has been developed for the volume electric energy, $W_E^{(V)} = n^2/2 \iiint \|\mathbf{E}(\mathbf{r},\lambda)\|^2 \,\mathrm{d}V$, using volume generated third harmonic emission,[19] we demonstrate here that the model can also be applied to surface effects, with the magnitude of the SH intensity, yielding a good measure of the electric energy stored at the dielectric surface.

We turn now our attention towards the study of the GaP nanoantenna as a nanophotonic platform optimized for the enhancement of radiative properties of fluorescent molecules in the visible range (schematic in Figure 3(a)). To that end, we built GaP dimer-like nanoantennas

with 35 nm gap size, as can be seen in the inset of Figure 3(a). The radius of the GaP pillars composing the antenna is 50 nm.

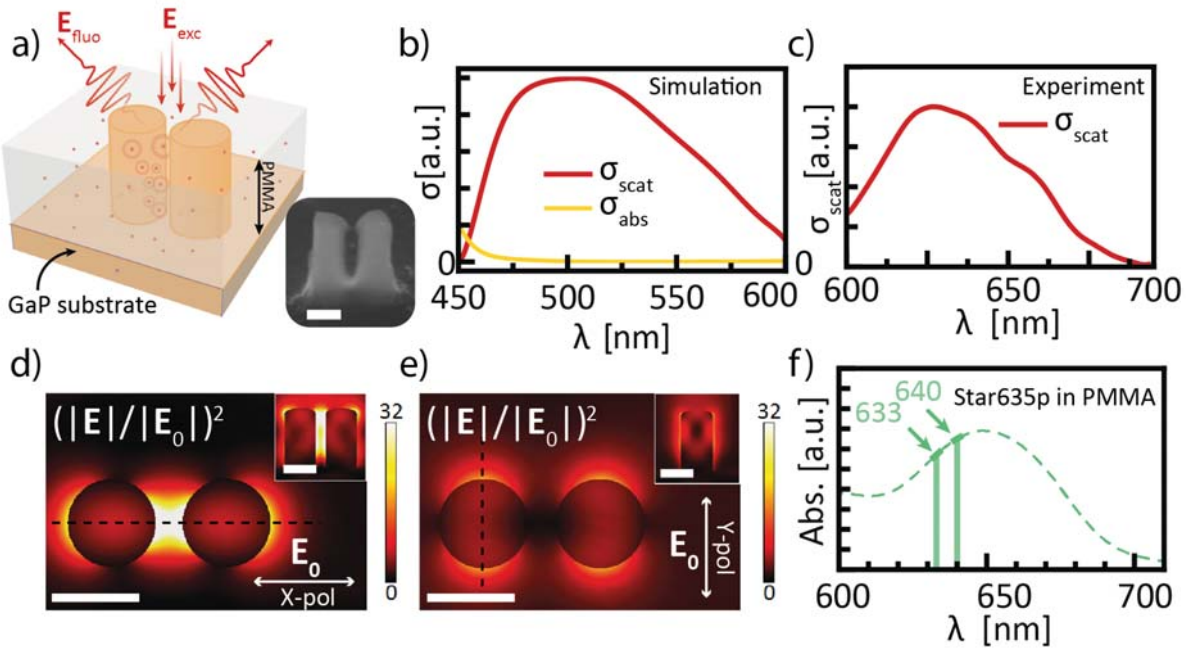

Figure 3: (a) Scheme of experimental configuration and scanning electron micrograph of a 35 nm gap GaP dimer. The scale bar is 100 nm. (b) Simulated scattering and absorption cross sections of the GaP nanoantenna in (a). (c) Experimental cross section of the antenna in (a). (d)-(e) Normalized electric field intensity distribution $\|\mathbf{E}(\mathbf{r},\lambda)\|^2/\|\mathbf{E}_0(\lambda)\|^2$ for excitation polarization X (d) and Y (e) computed at the simulated scattering maximum. The field is shown in the plane located at half the height of the antenna ($z = 100$ nm). The insets show the cross-section field distribution along the dashed lines. Scale bar: 100 nm. (f) Absorption spectrum of the fluorescent dye Star 635P measured in a solution of PMMA of 500 μM. The green vertical lines indicate the excitation wavelengths for photoluminescence experiments (633 nm) and time correlated experiments (640 nm).

To characterize the scattering resonances of the nanoantennas, we simulated and subsequently measured the scattering cross section of the designed GaP dimers, as shown, respectively, in Figures 3(b)-(c). A single broad peak can be seen in both cases in the selected spectral range, which would correspond to a dipolar mode, as deduced from the absence of other resonances at lower frequencies. The calculated absorption cross section of the nanoantenna, also included in Figure 3(b), is found to be nearly negligible at resonance, yielding a far-field scattering efficiency of 99%. We observe that this value highly contrasts with

the maximum radiation efficiency of about 75% simulated for a Si Yagi-Uda antenna in this spectral range,[2] anticipating the potential benefits of exploiting the close to zero absorption of GaP at visible wavelengths. In Figures 3(d)-(e) we plot the simulated electric field intensity distribution at resonance for both X and Y incident light polarization, *i.e.* parallel and perpendicular to the dimer orientation, respectively. As expected, the simulated patterns exhibit a dipolar behavior, giving rise to a field intensity enhancement factor of up to >32 for the X polarization. Conversely, this enhancement is only 10 when considering the perpendicular direction. Therefore, when the excitation light is polarized in the X direction, the gap region provides a suitable location for placing fluorescent molecules, with highly localized and enhanced fields.

To analyze the radiative properties of fluorophores in the gap of the GaP nanoantenna, we immersed the dielectric dimer, via spin coating, in a PMMA matrix containing Star 635P fluorescent dyes, which were chosen due to their negligible photobleaching rate.[47] The concentration of molecules was tuned to 500 μM, yielding an average of 50 fluorophores in the 35 nm gap. In Figure 3(f) we show the absorption spectrum of the fluorescent dye in the PMMA matrix, with the marked wavelengths indicating the excitation lasers used to probe the molecules, *i.e.* 633 nm (steady-state fluorescence experiments) and 640 nm (time-resolved fluorescence measurements).

To experimentally evaluate the SEF, the PMMA:dye coated nanoantenna was excited at resonance with linearly polarized 633 nm light at a power density of 2.5 MW cm^{-2}. The polarization of the excitation laser was chosen to be either parallel or perpendicular with the dimer's main axis. The fluorescence emission, characterized with a commercial WITec microscope, was collected in a back-scattering configuration, using a long-pass filter to remove the laser's contribution to the spectrum.

In Figure 4(a) we plot the fluorescence spectra registered when exciting the coated nanoantenna with the two different polarizations (I_{X} and I_{Y}), including, as reference, the result obtained when illuminating a bare PMMA:dye layer on the GaP substrate (I_{ref}). We

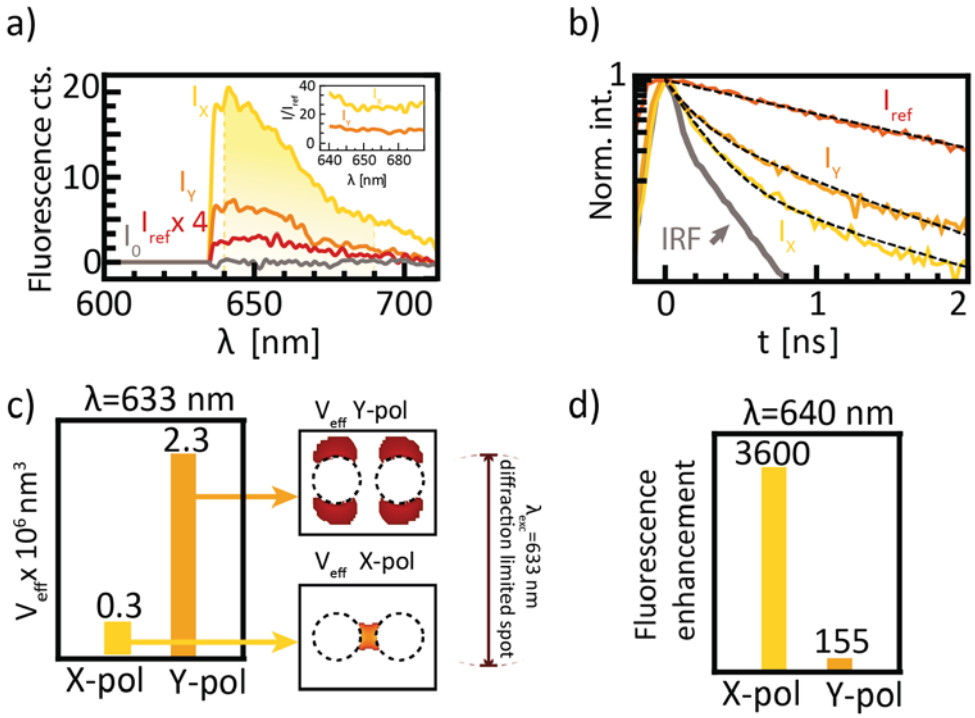

Figure 4: (a) Fluorescence spectra from the PMMA:dye coated 35 nm gap nanodimer excited at X and Y polarizations (I_{X} and I_{Y}, respectively), a region of molecules not interacting with the nanoantenna (I_{ref}) and bare PMMA/GaP (I_0), i.e. without the fluorescing molecule. The shaded area is inspected in the inset, where the counts are normalized to I_{ref} to obtain the increase in counts due to the presence of the nanoantenna for both polarization excitations. (b) Fluorescence emission decay rate curves together with the instrument response function (IRF). A bi-exponential model was used both for X and Y polarizations, however a single-exponential fit sufficed to describe the dynamics of the background. (c) Effective detection volumes used to calculate the enhancement factors in (b). The size of the used spot is also shown. The measured spot size coincided with the width of a focused gaussian spot (*i.e.* with an excitation spot radius of $\lambda/(\pi\mathrm{NA}) = 230$ nm, with NA the numerical aperture $NA = 0.9$). The volume of the spot interacting with the molecules is $(\lambda/(\pi\mathrm{NA}))^2\pi \times 200$ nm $= 3 \times 10^7$ nm^3. (d) Fluorescence enhancement factors, at 40 nm, calculated from Equation 1.

note that a bare PMMA film (*i.e.* containing no fluorescent dyes) on the GaP substrate produced only dark counts (I_0), indicating that the collected emission unequivocally corresponds to the Star 635P molecules. The inset of Figure 4(a) shows the relative increase of counts due to the presence of the antenna under X polarization ($I_{\mathrm{X}}/I_{\mathrm{ref}}$) and Y polarization ($I_{\mathrm{Y}}/I_{\mathrm{ref}}$) excitation. By analyzing the measured spectra, a clear polarization-dependent behavior can be observed when exciting fluorophores in the vicinity of the antenna. More specifically, for polarization parallel to the dimer's main axis, the emission intensity was found to be nearly three times that corresponding to the perpendicular polarization, and approximately 35 times that of the bare PMMA:dye mixture, excited at any polarization. It is necessary to mention here that these effective fluorescence enhancement factors do not yet take into account differences in the amount of molecules contributing to the emission in each case. Indeed, as it has been recently shown by fluorescence correlation experiments,[21] the effective excitation volume (V_{eff}), when considering resonant dimers excited with X polarization, corresponds to that defined by the gap size (V_{gap}), where the field is concentrated, whereas for measurements far from the antenna, V_{eff} is simply that of the diffraction-limited excitation spot (V_{spot}). A similar reasoning can be made for the Y polarization by considering the associated regions of enhanced fields. More details of effective volume calculations can be found in the SI, section 5. Figure 4(c) shows the effective excitation volumes predicted for our GaP dimer at each excitation polarization. Under these considerations, when the antenna is excited with polarization X/Y, the fluorescence enhancement factor ($\mathcal{F}_{\mathrm{X,Y}}$) can be calculated as:

$$\mathcal{F}_{\mathrm{X,Y}} = \frac{V_{\mathrm{spot}}}{V_{\mathrm{eff}}} \frac{I_{\mathrm{X,Y}}}{I_{\mathrm{ref}}} \tag{1}$$

where $I_{\mathrm{X,Y}}$ is the emission intensity measured when exciting at the antenna either parallel or perpendicularly, while I_{ref} corresponds to the signal registered when illuminating outside antenna regions. Remarkably, we obtain a value of $\mathcal{F}_{\mathrm{X}}$ as large as 3600 (Figure 4(d)). It is worth mentioning here that DNA origami approaches used to fine-tune the position of fluo-

rophores in ~ 10 nm gaps between Au colloids [48,49] led to $\mathcal{F}_X$ values of 5000. Noticeably, our approach provides comparable results, even though it uses considerably larger gap distances, demonstrating the advantage of employing an ultra-low loss dielectric nanoantenna. When switching to the Y polarization the enhancement factor drops to $\mathcal{F}_Y$ =144, in accordance with the reduced field-confinement capabilities of the nanoantenna in this situation (Figure 3(e)).

Regarding the decay rate of the fluorescence emission, it is intrinsically dependent on the localized density of optical states (LDOS). Qualitatively, the LDOS indicates the amount of states that can be excited by a local source at a given wavelength, [50] including both non-radiative modes and radiative (scattering) excitations. In the traditional case of a metallic nanostructure, even though the LDOS is strongly enhanced at the plasmonic resonance, inherent losses of the metal can induce large lifetime reductions of nearby emitters via the usually undesired non-radiative channels. [51] However, if the radiation efficiency of the nanoantenna is high, the reduction in the lifetime will be accompanied by an increase in the radiative rate of emission; a condition that can be met, in principle, with low-loss dielectrics. In this context, GaP presents as an excellent candidate in the visible range. We explore next the effect of the GaP dimer nanoantenna on the decay dynamics of the fluorescence probes.

Table 1: Fitting parameters for the lifetime decay curves in Figure 4(b). τ_0 is the decay time of the slow component, τ_1 the decay time of the fast component and $\Delta\tau$ is the FWHM of the IRF.

	Background	Y-pol	X-pol	IRF
τ_0 [ns]	1.10±0.01	1.10±0.01	1.10±0.01	-
τ_1 [ns]	-	0.12±0.01	<0.05	-
$\Delta\tau$ [ns]	-	-	-	0.180

Figure 4(b) shows time-resolved fluorescence measurements of the coated nanoantenna sample at 640 nm excitation wavelength, for the two different polarizations, parallel and perpendicular to the main dimer's axis. The optical response from the bare PMMA:dye film on the GaP substrate is also included. As predicted, a much faster decay is observed for the molecules interacting with the antenna, when compared to the case of the bare layer

of molecules. Furthermore, it can be seen that the fastest decay occurs when exciting the nanoantenna with the X polarization. In order to extract lifetime values from the measurements, we fit exponential decay functions to the data, convoluted with the instrument response function (IRF) (see SI, section 6). The characteristic time of the IRF, determined by its FWHM (full width half maximum), is 0.18 ns, allowing the determination of lifetime values of up to ∼0.05 ns.[21]

The fluorescence decay lifetimes obtained from the fittings are summarized in Table 1. A mono-exponential decay is observed for the bare dyes, yielding a total lifetime of 1.10 ns. Remarkably, in the presence of the GaP dimer, corresponding lifetime values are calculated to be as short as < 0.05 ns and 0.12 ns for X and Y excitation polarizations, respectively. In these two cases, the long lifetime component of 1.10 ns was also included in the fitting to account for background emission from dyes located outside of the enhanced-field regions. Indeed, for $t > 1$ ns in Figure 4(b), when fast processes vanish, the slopes of the decay curves are found to be nearly the same for all three considered situations.

It is important to remark that the shortest value of <0.05 ns in Table 1 cannot be accurately determined, as it falls well below the IRF characteristic time of 0.18 ns, and it is consequently limited by the instrument response. However, this provides us with a lower bound on the Purcell factor of 1.1 ns/0.05 ns ~ 22 when the excitation of the nanoantenna is optimum. It must be noted here that Si dimer nanoantennas with similar gap sizes have been reported to produce considerably smaller fluorescence enhancement and lifetime reduction, highlighting the importance of effectively lossless GaP against Si for 633 nm.[21]

In conclusion, we have explored the use of essentially lossless all-dielectric GaP nanosystems for visible light applications. We have investigated the manipulation of Mie-resonant modes to highly confine the electric field at the surfaces of the dielectric structure, benefiting two quintessential nanophotonic applications in the visible light regime, namely SHG and SEF. Starting with single individual NDs, we have studied their nonlinear SHG characteristics and found the highest yet reported SHG efficiency for a single nanostructure, to the

authors' knowledge, in the visible range. It has been further verified, by the experimental evidence of the spectral nonlinear response when changing the pump wavelength, that the observed SHG can be attributed to surface effects. When considering the linear optical regime, by exciting fluorescent dyes placed within a 35 nm gap of a GaP dimer nanoantenna, we have shown that a large fluorescence enhancement (3600) can be obtained. It is remarkable that this material shows such a strong fluorescent enhancement at relatively large gaps. In comparison, enhancement values of around 100 were reported for 30 nm gap Si dimers.[21] We explain this achievement as a direct consequence of the negligible absorption of GaP, which prevents it from enhancing non-radiative decay paths. A > 22 times lifetime reduction (limited by the IRF) in the fluorophores is obtained, indicating a strong near-field light-matter interaction of the emitter with the localized density of optical states. Engineering smaller gap GaP nanoantennas, or even other ubiquitous geometries commonly used in plasmonics,[52] might pave the way towards further improving field-confinement capabilities in the visible regime with practically lossless characteristics.

Supporting Information available

This material is available free of charge via the Internet at `http://pubs.acs.org`.

Refractive index of GaP and Si; fabrication and characterization of nanostructures; nanodisks and magnetic field distribution; second harmonic experimental setup; calculation of effective excitation volume; deconvolution of time-resolved plots and fits.

Acknowledgements

The authors declare no competing financial interests.The authors acknowledge the funding provided by the EPSRC Reactive Plasmonics Programme (EP/M013812/1), the ONR Global, the Royal Society (UF150542), the Lee-Lucas Chair in Physics and the Marie

Skłodowska-Curie actions Early Stage Researcher (J.C.) and Researcher Fellow (E.C.) programmes.

References

(1) West, P.; Ishii, S.; Naik, G.; Emani, N.; Shalaev, V.; Boltasseva, A. *Laser & Photonics Reviews* **2010**, *4*, 795–808.

(2) Krasnok, A. E.; Miroshnichenko, A. E.; Belov, P. A.; Kivshar, Y. S. *Opt Express* **2012**, *20*, 20599–604.

(3) Albella, P.; Poyli, M. A.; Schmidt, M. K.; Maier, S. A.; Moreno, F.; Sáenz, J. J.; Aizpurua, J. *The Journal of Physical Chemistry C* **2013**, *117*, 13573–13584.

(4) Novotny, L.; van Hulst, N. *Nat Photon* **2011**, *5*, 83–90.

(5) Khurgin, J. B. *Nature nanotechnology* **2015**, *10*, 2–6.

(6) Atwater, H. A.; Polman, A. *Nature materials* **2010**, *9*, 205–213.

(7) Brongersma, M. L.; Halas, N. J.; Nordlander, P. *Nature nanotechnology* **2015**, *10*, 25–34.

(8) Clavero, C. *Nature Photonics* **2014**, *8*, 95–103.

(9) Linic, S.; Aslam, U.; Boerigter, C.; Morabito, M. *Nature materials* **2015**, *14*, 567–576.

(10) Baffou, G.; Berto, P.; Bermúdez Ureña, E.; Quidant, R.; Monneret, S.; Polleux, J.; Rigneault, H. *ACS Nano* **2013**, *7*, 6478–6488.

(11) Knight, M. W.; Sobhani, H.; Nordlander, P.; Halas, N. J. *Science* **2011**, *332*, 702–704.

(12) Xie, W.; Walkenfort, B.; Schlücker, S. *J Am Chem Soc* **2013**, *135*, 1657–60.

(13) Cortés, E.; Xie, W.; Cambiasso, J.; Jermyn, A. S.; Sundararaman, R.; Narang, P.; Schlücker, S.; Maier, S. A. **2016**, arXiv:1607.05657.

(14) Manjavacas, A.; Liu, J. G.; Kulkarni, V.; Nordlander, P. *ACS Nano* **2014**, *8*, 7630–8.

(15) Kuznetsov, A. I.; Miroshnichenko, A. E.; Brongersma, M. L.; Kivshar, Y. S.; Luk'yanchuk, B. *Science* **2016**, *354*, aag2472.

(16) Caldarola, M.; Albella, P.; Cortés, E.; Rahmani, M.; Roschuk, T.; Grinblat, G.; Oulton, R. F.; Bragas, A. V.; Maier, S. A. *Nature communications* **2015**, *6*, 7915.

(17) Passaro, V. M.; Troia, B.; La Notte, M.; De Leonardis, F. *RSC Advances* **2013**, *3*, 25–44.

(18) Albella, P.; Alcaraz de la Osa, R.; Moreno, F.; Maier, S. A. *ACS Photonics* **2014**, *1*, 524–529.

(19) Grinblat, G.; Li, Y.; Nielsen, M. P.; Oulton, R. F.; Maier, S. A. *Nano Lett* **2016**, *16*, 4635–40.

(20) Alessandri, I.; Lombardi, J. R. *Chem Rev* **2016**, *116*, 14921–14981.

(21) Regmi, R.; Berthelot, J.; Winkler, P. M.; Mivelle, M.; Proust, J.; Bedu, F.; Ozerov, I.; Begou, T.; Lumeau, J.; Rigneault, H.; García-Parajó, M. F.; Bidault, S.; Wenger, J.; Bonod, N. *Nano Lett* **2016**, *16*, 5143–51.

(22) Brudny, V. L.; Mendoza, B. S.; Luis Mochán, W. *Phys. Rev. B* **2000**, *62*, 11152–11162.

(23) Berthelot, J.; Bachelier, G.; Song, M.; Rai, P.; des Francs, G. C.; Dereux, A.; Bouhelier, A. *Opt. Express* **2012**, *20*, 10498–10508.

(24) Canfield, B. K.; Kujala, S.; Jefimovs, K.; Turunen, J.; Kauranen, M. *Opt. Express* **2004**, *12*, 5418–5423.

(25) Zhang, Y.; Grady, N. K.; Ayala-Orozco, C.; Halas, N. J. *Nano Lett* **2011**, *11*, 5519–5523.

(26) Aouani, H.; Navarro-Cia, M.; Rahmani, M.; Sidiropoulos, T. P. H.; Hong, M.; Oulton, R. F.; Maier, S. A. *Nano Lett* **2012**, *12*, 4997–5002.

(27) Park, S.; Hahn, J. W.; Lee, J. Y. *Optics Express* **2012**, *20*, 4856–4870.

(28) Shcherbakov, M. R.; Neshev, D. N.; Hopkins, B.; Shorokhov, A. S.; Staude, I.; Melik-Gaykazyan, E. V.; Decker, M.; Ezhov, A. A.; Miroshnichenko, A. E.; Brener, I.; Fedyanin, A. A.; Kivshar, Y. S. *Nano Lett* **2014**, *14*, 6488–92.

(29) Shorokhov, A. S.; Melik-Gaykazyan, E. V.; Smirnova, D. A.; Hopkins, B.; Chong, K. E.; Choi, D.-Y.; Shcherbakov, M. R.; Miroshnichenko, A. E.; Neshev, D. N.; Fedyanin, A. A.; Kivshar, Y. S. *Nano Lett* **2016**, *16*, 4857–61.

(30) Camacho-Morales, R. et al. *Nano Lett* **2016**, *16*, 7191–7197.

(31) Shcherbakov, M. R.; Vabishchevich, P. P.; Shorokhov, A. S.; Chong, K. E.; Choi, D.-Y.; Staude, I.; Miroshnichenko, A. E.; Neshev, D. N.; Fedyanin, A. A.; Kivshar, Y. S. *Nano Lett* **2015**, *15*, 6985–6990.

(32) Yang, Y.; Wang, W.; Boulesbaa, A.; Kravchenko, I. I.; Briggs, D. P.; Puretzky, A.; Geohegan, D.; Valentine, J. *Nano Lett* **2015**, *15*, 7388–93.

(33) Jellison, G. E. *Optical Materials* **1992**, *1*, 151–160.

(34) Aspnes, D.; Kelso, S.; Logan, R.; Bhat, R. *Journal of applied physics* **1986**, *60*, 754–767.

(35) Rakic, A. D.; Djurisic, A. B.; Elazar, J. M.; Majewski, M. L. *Appl Opt* **1998**, *37*, 5271–83.

(36) Palik, E. D.; Ghosh, G. *Handbook of optical constants of solids*; Academic Press: San Diego, 1998.

(37) Rivoire, K.; Lin, Z.; Hatami, F.; Masselink, W. T.; Vucković, J. *Opt Express* **2009**, *17*, 22609–15.

(38) Sanatinia, R.; Swillo, M.; Anand, S. *Nano Lett* **2012**, *12*, 820–6.

(39) Sanatinia, R.; Anand, S.; Swillo, M. *Nano Lett* **2014**, *14*, 5376–81.

(40) Hayashi, S.; Koh, R.; Ichiyama, Y.; Yamamoto, K. *Phys Rev Lett* **1988**, *60*, 1085–1088.

(41) Goldberg, Y. In *Handbook series on semiconductor parameters*, world scientific ed.; Shur, M., Ed.; World Scientific: London, 1996; Vol. 1; pp 104–124.

(42) Liu, S.; Ihlefeld, J. F.; Dominguez, J.; Gonzales, E. F.; Bower, J. E.; Burckel, D. B.; Sinclair, M. B.; Brener, I. *Applied Physics Letters* **2013**, *102*, 161905.

(43) Gholipour, B.; Adamo, G.; Cortecchia, D.; Krishnamoorthy, H. N. S.; Birowosuto, M. D.; Zheludev, N. I.; Soci, C. *Adv Mater* **2017**, 1604268.

(44) Kronawitter, C. X.; Lessio, M.; Zahl, P.; Muñoz-García, A. B.; Sutter, P.; Carter, E. A.; Koel, B. E. *The Journal of Physical Chemistry C* **2015**, *119*, 28917–28924.

(45) Gennaro, S. D.; Rahmani, M.; Giannini, V.; Aouani, H.; Sidiropoulos, T. P. H.; Navarro-Cía, M.; Maier, S. A.; Oulton, R. F. *Nano Lett* **2016**, *16*, 5278–85.

(46) Grinblat, G.; Rahmani, M.; Cortés, E.; Caldarola, M.; Comedi, D.; Maier, S. A.; Bragas, A. V. *Nano Lett* **2014**, *14*, 6660–5.

(47) Wu, Y.; Wu, X.; Lu, R.; Zhang, J.; Toro, L.; Stefani, E. *Scientific Reports* **2015**, *5*, 14766.

(48) Puchkova, A.; Vietz, C.; Pibiri, E.; Wünsch, B.; Sanz Paz, M.; Acuna, G. P.; Tinnefeld, P. *Nano Lett* **2015**, *15*, 8354–8359.

(49) Bidault, S.; Devilez, A.; Maillard, V.; Lermusiaux, L.; Guigner, J.-M.; Bonod, N.; Wenger, J. *ACS Nano* **2016**, *10*, 4806–15.

(50) Novotny, L.; Hecht, B. *Principles of Nano-Optics*, 2nd ed.; Cambridge, 2012.

(51) Anger, P.; Bharadwaj, P.; Novotny, L. *Phys Rev Lett* **2006**, *96*, 113002.

(52) Lindquist, N. C.; Nagpal, P.; McPeak, K. M.; Norris, D. J.; Oh, S.-H. *Reports on Progress in Physics* **2012**, *75*, 036501.

Graphical TOC Entry